Check for updates

*Magnetic Resonance in Medicine*

WILEY | ISMRM ONE COMMUNITY FOR CLINICIANS AND SCIENTISTS

RESEARCH ARTICLE OPEN ACCESS

# $B_1^+$ Optimization in the Heart at 7 T

Erin McConnell Montoya[1] | Aaron T. Hess[2] | Damian J. Tyler[1,3] | Ladislav Valkovič[1,4]

[1]Oxford Centre for Clinical MR Research (OCMR), RDM Cardiovascular Medicine, University of Oxford, Oxford, UK | [2]Oxford Centre for Integrative Neuroimaging (OxCIN), Nuffield Department of Clinical Neurosciences, University of Oxford, Oxford, UK | [3]Department of Physiology, Anatomy and Genetics, University of Oxford, Oxford, UK | [4]Department of Imaging Methods, Institute of Measurement Science, Slovak Academy of Sciences, Bratislava, Slovakia

**Correspondence:** Ladislav Valkovič (ladislav.valkovic@cardiov.ox.ac.uk)

**Received:** 4 June 2026 | **Revised:** 16 October 2026 | **Accepted:** 5 November 2026

**Keywords:** $B_1^+$ | 7 T | cardiac imaging | optimization | shimming

## ABSTRACT

**Purpose:** At 7 T, the short RF wavelength in tissue (~11 cm) causes destructive interference within the chest, leading to $B_1^+$ inhomogeneity and posing a critical challenge for cardiac MRI and MRS. While subject-specific parallel-transmit (pTx) optimization can mitigate this, it requires calibration scans and offline computation. To simplify this process, a static "global" shim was calculated and demonstrated to outperform the default transmit configuration without participant-specific calibration.

**Methods:** $B_1^+$ maps were acquired in 12 healthy volunteers at 7 T using an 8-channel $^1$H torso coil. "Personal" phase-only shims were calculated per subject by minimizing a cost function of $B_1^+$ homogeneity and efficiency. The "global" shim was calculated by optimizing performance across the cohort, then validated in six additional volunteers by comparing performance against the native mode.

**Results:** In the validation cohort, the "global" significantly outperformed the native shim. It increased the Mean Transmit Sensitivity by ~20% and reduced CoV by ~ 16% in the septum. The fixed global shim performance was within 3% of the computationally expensive personal shim for all metrics.

**Conclusion:** A fixed, population-derived, global phase shim provides a practical, calibration-free approach for improving cardiac $B_1^+$ performance at 7 T. The present results extend previous universal RF-shimming work through prospective evaluation in an independent validation cohort and demonstrate that much of the benefit of personal shimming can be retained without participant-specific optimization. The resulting fixed-phase configuration could also provide a practical route towards implementation on single-transmit hardware for cardiac imaging and spectroscopic applications.

## 1 | Introduction

Ultra-high field strengths (i.e., 7 T and above) can offer higher SNR and hence faster scan times or higher spatial resolutions when compared to clinical field strengths (i.e., 1.5/3 T). The move to higher field strengths, however, compromises the homogeneity and efficiency of the transmit $B_1^+$ field. The short RF wavelength at 7 T (~11 cm in tissue) results in unwanted variations in flip-angles within scanned organs, and is particularly challenging for cardiac applications, causing banding artifacts in cardiac imaging and distorting localization schemes in cardiac spectroscopy, introducing bias in quantified concentrations and increasing inter-scan variability [1]. At 7 T, transmit performance is further constrained by RF power limits and SAR considerations, motivating shim strategies that improve flip-angle efficiency without increasing peak power. Importantly, transmit-field behavior in the heart is highly subject-dependent due to variations in cardiac geometry and surrounding tissue

This is an open access article under the terms of the Creative Commons Attribution License, which permits use, distribution and reproduction in any medium, provided the original work is properly cited.

© 2026 The Author(s). *Magnetic Resonance in Medicine* published by Wiley Periodicals LLC on behalf of International Society for Magnetic Resonance in Medicine.

composition, so shim solutions must be generalizable across all anatomies, including those which are clinically relevant.

Standard single-transmit (sTx) configurations, constrained by sub-optimal fixed phase relationships, fundamentally cannot correct the complex constructive and destructive interference patterns, prominent at 7 T. Parallel transmit (pTx) arrays provide the independent channels necessary to steer these interference patterns. However, whilst pTx arrays offer the degrees of freedom needed to improve the homogeneity of the $B_1^+$ field at 7 T [2], their broader practical use in cardiac MRI has often been limited by workflows that rely on personal calibration and optimization. In standard active shimming workflows, calibration data must be acquired, exported and processed to derive the optimal shim weights for each participant. While rapid acquisition techniques for B1 mapping have been recently proposed [3], and processing algorithms are getting faster, this iterative process still introduces significant "dead time," hindering one of the potential benefits of 7 T, that is, faster scans. Additionally, assuming that personal optimization is only done once, the concept of a personal shim relies on the unlikely circumstance that a participant's anatomy-to-coil orientation remains unchanged during the whole scan session or between scan sessions (anterior coil elements are normally placed directly on the chest and may therefore occupy a slightly different position relative to the heart following participant repositioning between scan sessions). Non-subject-specific pTx approaches have also been explored, including radio-frequency simulation of default global shim settings [4], calibration-free universal pulse design [5], universal RF-shimming and pulse-design approaches evaluated in the heart and prostate [6] and universal shim modes for spinal cord imaging [7]. Calibration-free static RF shims have also been demonstrated for predefined brain spectroscopy regions, where they produced $B_1^+$ performance and spectral quality comparable with tailored shimming without requiring participant-specific calibration [8]. Egger et al. [6] derived and retrospectively evaluated universal phase shims using measured channel-wise cardiac $B_1^+$ maps from a large cohort, although prospective in vivo validation of the universal cardiac shim was only demonstrated in a single participant. More broadly, prospective evidence supporting a single fixed cardiac shim that can be used without personal optimization remains limited.

The distinction is particularly important for cardiac spectroscopy. Many X-nuclei sequences, for example, phosphorus ($^{31}$P) spectroscopy, often remain restricted to sTx modes due to system architecture or specific coil designs. In these "hardware-combined" configurations, the relative phases of the coil elements are fixed by the cabling and power splitter. Hence personal optimization is impossible in practice, as it would require physically changing cable lengths for each participant. Therefore, determining an optimized, fixed-phase global shim is not merely a workflow convenience, but a practical route for translating high-field homogeneity and transmit efficiency gains to X-nuclei spectroscopy on systems without pTx enabled. More broadly, several strategies have been explored to mitigate $B_1^+$ inhomogeneity at 7 T. Passive shimming using high-dielectric pads can locally enhance field transmission [9], but this adds logistical complexity and variability to patient setup. Static $B_1^+$ shimming therefore remains an attractive approach for cardiac applications; however, the necessity of performing this optimization on a per-subject basis continues to hinder high-throughput workflows.

The aim of this study was to assess the feasibility of deriving a single fixed, phase-only global RF shim that could be applied on a pTx system without personal calibration and that could, in principle, be implemented as a fixed combined transmit mode for sTx operation. Building directly on the work of Egger et al., and using a different coil and experimental setup, the present study extends the prospective evaluation of universal ("global") phase-only cardiac RF shimming to an independent cohort, with assessment across repeat sessions and within whole-heart, intraventricular septal, and spectroscopy-voxel ROIs. The global shim was evaluated for its ability to improve transmit efficiency and $B_1^+$ homogeneity within the whole heart for MRI applications and within the intraventricular septum for MRS applications.

## 2 | Methods

### 2.1 | Study Design

In this study, a cohort of 12 healthy volunteers (7 male, 5 female; age $31.4 \pm 11.2$ years, BMI $24.4 \pm 3.7\,\mathrm{kg/m^2}$) were scanned for the initial optimization stage; which we shall call the "first scan session." Shims were then computed based on these 12 anatomies individually to create "personal" shims, and together to create a "global" shim. These personal and global shims were then reapplied to each participant later, in a "second scan session." Performance was simulated using the personal and global shims on both the first and second scan sessions' field maps, and evaluated using vendor-constructed maps taken directly from the scanner. The global shim was subsequently applied to an additional 6 volunteers to validate the improvements. All participants were scanned according to an institutionally-approved technical development standard operating procedure.

#### 2.1.1 | $B_1^+$ Field Definitions

To bridge the gap between field mapping and imaging, it is necessary to define the relationship between the two. The transmit field efficiency ($B_1^+$) directly impacts the resultant signal in MRI and MRS. The flip angle $\alpha$ achieved at any position $\mathbf{r}$ is proportional to the local $B_1^+$ field strength and the duration of the RF pulse $\tau$. To characterize this relationship, we calculated the mean transmit sensitivity (or mean $|\,B_1^+\,|$) in units of Hz/V. This metric describes the scanner's ability to nutate spins for every volt of input power. A higher sensitivity means the required flip angle can be reached using less voltage, directly reducing the SAR (specific absorption rate). We also characterized the RF performance by evaluating the shim efficiency (or transmit efficiency), which assesses the phase coherence of the array. Ultimately, the final flip angle is determined by the product of the transmit sensitivity and the input voltage. If the sensitivity is low (e.g., due to poor $B_1$ shim efficiency), the pulses may fail to reach the required flip angle, causing a loss in signal intensity proportional to the number of pulses.



15222594, 0, Downloaded from https://onlinelibrary.wiley.com/doi/10.1002/mrm.70670, Wiley Online Library on [18/11/2026]. See the Terms and Conditions (https://onlinelibrary.wiley.com/terms-and-conditions) on Wiley Online Library for rules of use; OA articles are governed by the applicable Creative Commons License

### 2.1.2 | Optimization

The combined $B_1^+$ field from all transmit channels can be expressed as:

$$B_{\text{shim}}(r) = \sum_{c=1}^{N_{\text{Ch}}} \omega_c \cdot b_c(r) \tag{1}$$

where $\omega_c$ is the complex shim weight per channel $c$ and $b_c(r)$ is the complex transmit sensitivity map per channel $c$. Phase-only shimming was implemented such that $|\ \omega_c\ | = 1$ by parametrizing $\omega_c = e^{i\theta_c}$; ensuring equal channel amplitudes whilst allowing constructive and destructive through phase variation. No explicit local SAR minimization was included in the optimization because subject-specific electromagnetic simulations, Q-matrices, and VOP constraints were not available. The optimization was phase-only, with equal and fixed channel amplitudes, and therefore did not alter the prescribed power on any individual transmit channel. Safety supervision was instead based on the scanner's conservative worst-case per-channel power limits, which were independent of the applied phase vector, and all scans were performed within the scanner-reported safety limits [10].

The loss function maximized the mean $B_1^+$ magnitude, whilst reducing spatial inhomogeneity (coefficient of variation [CoV]):

$$l = \frac{1}{\overline{B}} + \lambda_{\text{cov}} \cdot \frac{\sigma_B}{\overline{B}} \tag{2}$$

where $B(r) = |\ B_{\text{shim}}(r)\ |$ denotes the magnitude of the shimmed $B_1^+$ field at spatial location $r$ within the ROI. $\overline{B}(r)$ denotes the mean $B(r)$ across the ROI, $\sigma_B$ denotes its standard deviation, and $\frac{\sigma_B}{\overline{B}}$ therefore represents the CoV within the ROI. $\lambda_{cov}$ is a weighting parameter governing the trade-off between homogeneity and transmit efficiency. The first term in Equation (2) maximizes transmit efficiency (effectively the average flip angle), whilst the second term minimizes the CoV to improve spatial homogeneity, and $\lambda_{\text{cov}}$ controls the trade-off between transmit efficiency and homogeneity. The weighting was fixed at $\lambda_{\text{cov}} = 0.5$ for all personal and global optimizations. This relatively low value was selected to prioritize $B_1^+$ efficiency while retaining a modest homogeneity constraint. As shown in the Figure S1, CoV varied comparatively little across the tested $\lambda_{\text{cov}}$ values, whereas higher values placed greater emphasis on homogeneity at the expense of mean $B_1^+$. A low weighting was therefore retained to favor transmit efficiency without materially compromising homogeneity.

Numerical minimization was performed in MATLAB using a multi-start phase-only optimization. The complex shim weights were constrained to $\omega_c = e^{i\theta_c}$, with the first channel phase fixed to zero to remove the arbitrary global phase offset. A coarse grid search consisting of 10 equally spaced phases on each of seven remaining channels, giving $10^7$ test locations. The 50 lowest-loss seed vectors were then refined using the Nelder–Mead simplex algorithm implemented with `fminsearch`. This grid-based initialization was chosen to sample the available phase space uniformly rather than relying on a limited number of randomly selected starting points. Similar pre-selection of starting phase vectors has previously been shown to increase the probability of identifying the global optimum in phase-only transmit-array optimization [4]. Because optimization was performed offline, computational speed was considered less important than broad phase-space coverage and robustness to local minima. The final shim was selected as the refined solution with the lowest loss, and its phases were wrapped to $[-180^\circ, 180^\circ]$ for reporting. The same optimization strategy was used for both personalized and global shims. For personalized shimming, the loss was evaluated within each subject's ROI. For the global shim, the objective function was evaluated across the cohort. For each candidate phase vector, the mean $B_1^+$ magnitude, $\overline{B}_s$, and CoV, $\text{CoV}_s$, were calculated separately for each subject. The group loss was defined as:

$$l_{\text{group}} = \frac{1}{\frac{1}{N_s}\sum_{s=1}^{N_s} \overline{B}_s} + \lambda_{\text{cov}} \left( \frac{1}{N_s} \sum_{s=1}^{N_s} \text{CoV}_s \right), \tag{3}$$

where $N_s$ is the number of subjects. This approach ensured that the global shim was optimized using subject-level metrics rather than by concatenating all ROIs into a single mask, avoiding bias towards subjects with larger ROIs. The best shim vector is selected as:

$$\omega_{\text{opt}} = e^{i\theta_{\text{opt}}} \tag{4}$$

where $\theta_{\text{opt}}$ corresponds to the minimum loss among all local optimizations. Using the optimal shim weights $\omega_{\text{opt}}$, the shimmed combined $B_1^+$ field (transmit sensitivity) was reconstructed via:

$$B_{1,\text{shim}}^+(r) = \sum_{c=1}^{N_{\text{Ch}}} \omega_{\text{opt},c} . B_{1,c}^+(r) \tag{5}$$

And the following performance metrics were evaluated: $|\ \overline{B_1^+}\ |$, median $|\ B_1^+\ |$, CoV of the $B_1^+$ field and shim efficiency ($\overline{\eta}$), given by:

$$\eta(r) = \frac{|\ B_{\text{shim}}^+(r)\ |}{\sum_{c=1}^{N_{\text{Ch}}} |\ B_{1,c}^+(r)\ |} \tag{6}$$

Which is a measure of how close the shim comes to the ideal constructive interference. A low shim efficiency indicates that significant energy is being lost due to destructive interference between channels. Figures S2 and S4 display the absolute and actual phase differences between each of the personal shims for each of the eight transmit channels. Figures S3 and S5 display the per-channel absolute and actual phase differences between each personal shim and the global shim.

## 2.2 | In Vivo Experiments

During the first scan session, the 4D (3D volume × N channel) complex $B_1^+$ maps of 12 healthy volunteers were obtained during free-breathing using the $B_1$-sandwich method described by Kent et al. [3]. The maps were acquired with 3D spatial encoding at a spatial resolution of $5 \times 5 \times 5\,\text{mm}^3$ and a field of view of $400 \times 300 \times 240\,\text{mm}^3$ on a 7 T Siemens Magnetom Plus scanner (Siemens Healthineers, Erlangen, Germany) running in pTx mode. PTx mode allowed for real-time alterations of the individual coil element phases. Two $B_1^+$ transmit encoding modes were acquired, with GRAPPA (acceleration factor = 4). Each map required 4.5 min to acquire; including localizers, the



15222594, 0, Downloaded from https://onlinelibrary.wiley.com/doi/10.1002/mrm.70670, Wiley Online Library on [18/11/2026]. See the Terms and Conditions (https://onlinelibrary.wiley.com/terms-and-conditions) on Wiley Online Library for rules of use; OA articles are governed by the applicable Creative Commons License

total scan time was 10 min. The acquisition parameters were: TR = 96 ms, TE = 0.59 ms, nominal flip-angle = 4.0° [3]. Volunteers were scanned in a head-first supine position, using an eight-channel $^{1}$H torso coil featuring a transmit/receive dipole antenna array (MR Coils, Zaltbommel, The Netherlands). The relative geometry of the dipole elements is described in [11], although the array is illustrated there in a pelvic rather than thoracic configuration. Cardiac triggering for the $B_1^+$ mapping acquisition was performed using pulse oximetry. Because the peripheral pulse trigger occurs later in the cardiac cycle than the ECG R-wave [12], the acquisition delay was reduced to approximately 100 ms to maintain acquisition within diastole. $B_1^+$ data were reconstructed from individual channel complex sensitivity maps. Metadata, including transmit voltage settings and scaling factors, were extracted from machine readable JSON files associated with each scan. These parameters were used to normalize the raw signal intensities, ensuring that the resulting maps represented the physical $|B_1^+|$ field in units of Hz/V. The shimmed $B_1^+$ field was then calculated as the complex weighted sum of the $N$ individual-channel maps, allowing direct comparison of shim performance across participants. Binary masks were created using FSLeyes [13] for each volunteer for an ROI of the whole heart, an ROI covering the intraventricular septum and an ROI that simulated a single spectroscopy voxel along the intraventricular septum ($20 \times 20 \times 40\ mm^3$). No spatial filtering, interpolation or smoothing was applied to the $B_1^+$ maps prior to optimization. Voxels with nonfinite or zero $B_1^+$ values in any of the eight individual-channel maps were excluded during ROI curation and were not interpolated or replaced. Map quality was additionally assessed by calculating the proportion of voxels within each optimization ROI for which finite, nonzero complex $B_1^+$ values were present across all eight transmit channels. MATLAB (R2024b) code following the theory outlined in Section 2.1.2 was used to optimize the mean and median $B_1^+$, CoV and shim efficiency within the whole-heart ROI. Spatial homogeneity was assessed via CoV, since spatial $B_1^+$ variations cause flip-angle errors that degrade slice-selective profile sharpness and thereby reduce the fidelity of voxel localization. The septum and voxel masks were subsequently utilized to evaluate shim performance in specific anatomical regions, simulating the requirements for localized MRS. Group optimization used un-normalized $B_1^+$ maps to preserve inter-subject differences in absolute efficiency; favoring a cohort-robust shim maximizing $|B_1^+|$ whilst penalizing CoV. Both the personal and global shim solutions were evaluated via numerical simulations offline. For each subject, the shim efficiency ($\overline{\eta(r)}$), CoV, and the mean and median $|B_1^+|$ magnitude within the whole-heart ROI were computed and compared with the scanner native shim configuration: $\omega_0 = [0, 0, 0, 0, 0, 0, 0, 0]^\circ$. To assess the robustness of the personal shim across separate scan sessions, we analyzed them when reapplied to the same participants using updated field maps. These metrics reflect an offline optimization approach, incorporating the anatomical shifts and positional discrepancies relative to the coil that could occur between the initial optimization and the cardiac scans in case of participant motion. To qualitatively evaluate shimming performance, simulated $|B_1^+|$ maps were generated via Equation (5) for the native shim ($\omega_0$), the global solution ($\omega_g$) and the personal shim ($\omega_p$). We validated this approach by reacquiring complex $B_1^+$ maps in the same 12 volunteers (second scan session) using both $\omega_p$ and $\omega_g$, the latter also applied in an additional 6 volunteers. To assess the performance of $\omega_p$ and $\omega_g$, vendor-constructed real $B_1^+$ maps reconstructed on the scanner were converted into units of Hz/V and compared under each shim setting.

To determine the requirements for a robust and generalizable global shim, the impact of cohort size was evaluated. $B_1^+$ maps from the second session were used for simulation (the personal shims were not derived from these maps). For each participant, training cohorts were constructed by randomly ordering the remaining 11 participants, necessarily excluding the participant's own anatomy. Group shims were then calculated after incrementally adding participants according to this order.

To quantify the impact of global shimming on image quality, cardiac CINE images were acquired for one participant with both $\omega_0$ and $\omega_g$ applied. A standardized ROI-based Contrast-to-Noise Ratio (CNR) analysis was performed across the full cardiac cycle (20 frames). For each frame, fixed-sized $5 \times 5$ pixel ROIs were manually placed in the left ventricular blood pool and the intraventricular septum. CNR was calculated as the absolute difference between the mean signal intensities of the blood and myocardium, normalized by the myocardial standard deviation. This was evaluated for all 20 frames to evaluate the temporal stability of the shim throughout the entire cardiac cycle.

Additional post-processing analyses were performed to assess the dependence of global-shim performance on the optimization ROI and participant sex. First, a septum-derived global shim was generated by applying the same group optimization procedure within the intraventricular septum across the optimization cohort and was compared with the whole-heart-derived global shim within the septal ROI. Second, sex-specific global shims were generated separately for the male ($n = 7$) and female ($n = 5$) participants in the optimization cohort, applied in vivo, and compared with the population-derived global shim within the whole-heart, septal and spectroscopy-voxel ROIs.

## 2.3 | Statistical Analysis

Statistical analysis was performed in Python (v3.11) using the SciPy library. The normality of differences between shimming configurations (e.g., $[|\overline{B_1^+}|$ using $\omega_p)$—$(|\overline{B_1^+}|$ using $\omega_0])$ was evaluated for each performance metric using the Shapiro–Wilk test for both simulations and in vivo analysis. The percentage changes are quoted with their SEM (Standard error of the mean, $SEM = \frac{\sigma}{\sqrt{n}}$ where $\sigma$ is the standard deviation of the sample and $n$ is the sample size). For metrics where the differences were normally distributed ($p > 0.05$), a paired-samples $t$-test was employed as the primary measure of statistical significance. In cases where the Shapiro–Wilk test indicated significant nonnormality ($p < 0.05$), the nonparametric Wilcoxon signed-rank test was prioritized. Additionally, to ensure the robustness of the findings across the small sample sizes, all comparisons were cross-validated using the Wilcoxon signed-rank test, even when normality assumptions were met. All statistical tests were two-tailed, and significance was defined at the $p < 0.05$ level to provide a conservative estimate of shim performance improvements. Unless stated otherwise; $p$ values reported in the results correspond to paired $t$-tests.



15222594, 0, Downloaded from https://onlinelibrary.wiley.com/doi/10.1002/mrm.70670, Wiley Online Library on [18/11/2026]. See the Terms and Conditions (https://onlinelibrary.wiley.com/terms-and-conditions) on Wiley Online Library for rules of use; OA articles are governed by the applicable Creative Commons License

## 3 | Results

### 3.1 | Optimization

Representative coronal (Figure 1a–c) and sagittal (Figure 1d–f) simulated $|B_1^+|$ maps from a single participant are shown in Figure 1. Qualitatively, both the global and personal shims demonstrated a visible increase (Figure 1b–f) in $|B_1^+|$ and a reduction in the destructive interference patterns (shading) observed when using the scanner native mode (Figure 1a,d) within the whole-heart ROI. Across the 30 individual-channel $B_1^+$ maps, the valid-voxel yield was 97.3% ± 2.7%, ranging from 86.75% to 99.97%. Table 1 reports group-averaged improvements in the simulated transmit field performance metrics within the whole-heart ROI across the 12 participants in the first scan session. $\omega_p$ and $\omega_g$ were compared with the native shim (first two blocks), and then with each other (last block). Quantitative analysis of the transmit field metrics demonstrated that both global and personal shimming strategies yielded highly significant improvements over the scanner native mode across most evaluation metrics ($p < 0.001$ for both paired $t$-tests and Wilcoxon tests). Compared to $\omega_0$, $\omega_g$ increased mean $|B_1^+|$ by 14.6% ± 2.0% and shim efficiency by 14.1% ± 1.9%. Similarly, $\omega_p$ resulted in gains of 17.7% ± 2.0% in Mean $|B_1^+|$ and 17.1% ± 1.9% in shim efficiency over $\omega_0$. Within the whole heart ROI, field homogeneity was not significantly altered by either optimized shim. A secondary analysis was performed to compare the two optimized shimming strategies directly. While both methods were superior to the native shim, $\omega_p$ demonstrated specific statistical advantages in all metrics except CoV. The personal shim provided a modest, yet statistically significant increase in Mean transmit sensitivity $|\overline{B_1^+}|$ (2.75 ± 0.46%, $p < 0.0001$), Mean transmit efficiency (2.68% ± 0.41%, $p < 0.0001$), and Median $|B_1^+|$ (1.67% ± 0.71%, $p = 0.033$) compared to the global shim ($\omega_g$). No significant difference was observed between the two strategies regarding field homogeneity (CoV, $p = 0.54$). Tables S1 and S3 display septal and voxel-ROI results from the first scan session.

**TABLE 1** | Performance metrics from simulations from the first scan session.

| Metric | (Δ, %) |
|---|---|
| $\omega_p - \omega_0$ | |
| $\lvert\overline{B_1^+}\rvert$ | 0.00877 ± 0.00087 Hz/V, 17.7% ± 2.0% |
| Median $\lvert B_1^+\rvert$ | 0.0089 ± 0.0013 Hz/V, 19.9% ± 2.8% |
| CoV | −0.55% ± 0.69%, −0.9% ± 1.7% |
| $\overline{\eta}(\mathbf{r})$ | 11.1% ± 1.2%, 17.1% ± 1.9% |
| $\omega_g - \omega_0$ | |
| $\lvert\overline{B_1^+}\rvert$ | 0.00716 ± 0.00093 Hz/V, 14.6% ± 2.0% |
| Median $\lvert B_1^+\rvert$ | 0.0080 ± 0.0012 Hz/V, 17.9% ± 2.6% |
| CoV | 0.04% ± 0.78%, 1.0% ± 1.9%% |
| $\overline{\eta}(\mathbf{r})$ | 9.1% ± 1.2%, 14.1% ± 1.9%% |
| $\omega_p - \omega_g$ | |
| $\lvert\overline{B_1^+}\rvert$ | 0.00160 ± 0.00025 Hz/V, 2.75% ± 0.46% |
| Median $\lvert B_1^+\rvert$ | 0.00091 ± 0.00037 Hz/V, 1.67% ± 0.71% |
| CoV | −0.51% ± 0.81%, −1.5% ± 2.3% |
| $\overline{\eta}(\mathbf{r})$ | 1.97% ± 0.29%, 2.68% ± 0.41%% |

*Note:* Changes with "personal" (P) and "global" (G) shims relative to the scanner native (nat) system shim within the whole-heart ROI are shown. Absolute changes are reported alongside relative percentage changes. Values represent averages across the 12 participants included in the optimization cohort.

Table 2 summarizes the simulated performance of the personal and global shims when reapplied to the same participants in the second scan session. Normality testing again confirmed that the majority of the differences in performance metrics were

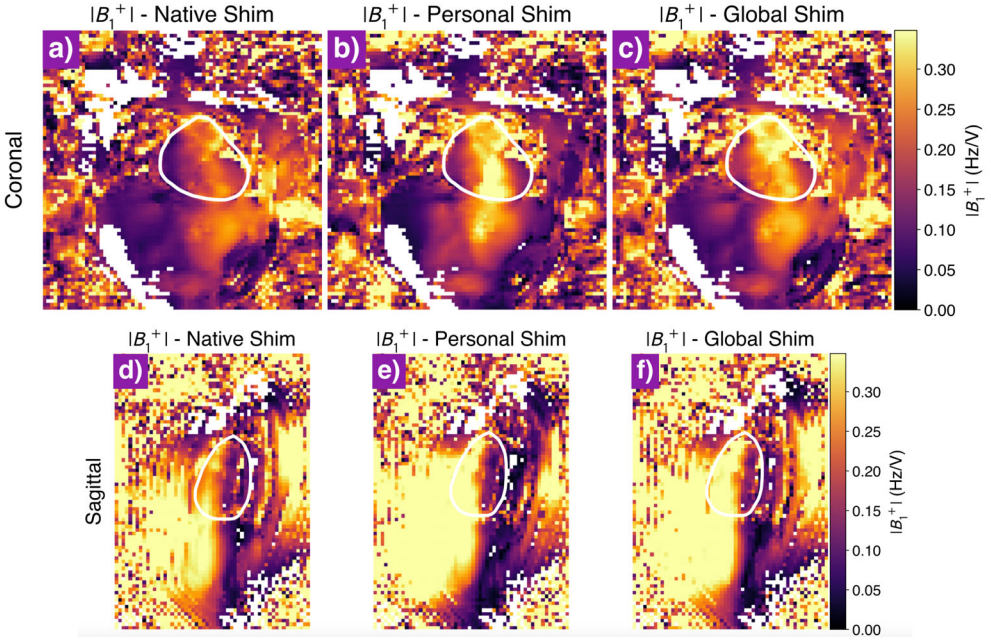



**FIGURE 1** | Representative coronal and sagittal $|B_1^+|$ maps with (a), (d) native shim, (b), (e) "personal" shim and (c), (f) "global" shim. White line encloses whole-heart ROI.



15222594, 0, Downloaded from https://onlinelibrary.wiley.com/doi/10.1002/mrm.70670, Wiley Online Library on [18/11/2026]. See the Terms and Conditions (https://onlinelibrary.wiley.com/terms-and-conditions) on Wiley Online Library for rules of use; OA articles are governed by the applicable Creative Commons License

**TABLE 2** | Performance metrics from simulations from the second scan session.

| Metric | (Δ, %) |
|---|---|
| $\omega_p - \omega_0$ | |
| $\lvert \overline{B_1^+} \rvert$ | 0.00516 ± 0.00068 Hz/V, 11.8% ± 1.5% |
| Median $\lvert B_1^+ \rvert$ | 0.00669 ± 0.00096 Hz/V, 15.9% ± 1.9% |
| CoV | −0.4% ± 1.6%, −1.0% ± 3.8% |
| $\overline{\eta}(\mathbf{r})$ | 8.22% ± 0.86%, 12.3% ± 1.4% |
| $\omega_g - \omega_0$ | |
| $\lvert \overline{B_1^+} \rvert$ | 0.00590 ± 0.00047 Hz/V, 13.6% ± 1.1% |
| Median $\lvert B_1^+ \rvert$ | 0.00737 ± 0.00077 Hz/V, 17.6% ± 1.5% |
| CoV | −1.27% ± 0.77%, −3.6% ± 1.9% |
| $\overline{\eta}(\mathbf{r})$ | 9.47% ± 0.59%, 14.2% ± 0.93% |
| $\omega_p - \omega_g$ | |
| $\lvert \overline{B_1^+} \rvert$ | −0.00073 ± 0.00038 Hz/V, −1.55% ± 0.71% |
| Median $\lvert B_1^+ \rvert$ | −0.00068 ± 0.00044 Hz/V, −1.49% ± 0.84% |
| CoV | 0.9% ± 1.1%, 2.5% ± 2.9% |
| $\overline{\eta}(\mathbf{r})$ | −1.25% ± 0.48%, −1.62% ± 0.66% |

*Note:* Changes with "personal" (P) and "global" (G) shims relative to the system native (nat) shim mode within the whole-heart ROI are shown. Absolute changes are reported alongside relative percentage changes. Values represent averages across the 12 participants included in the optimization cohort.

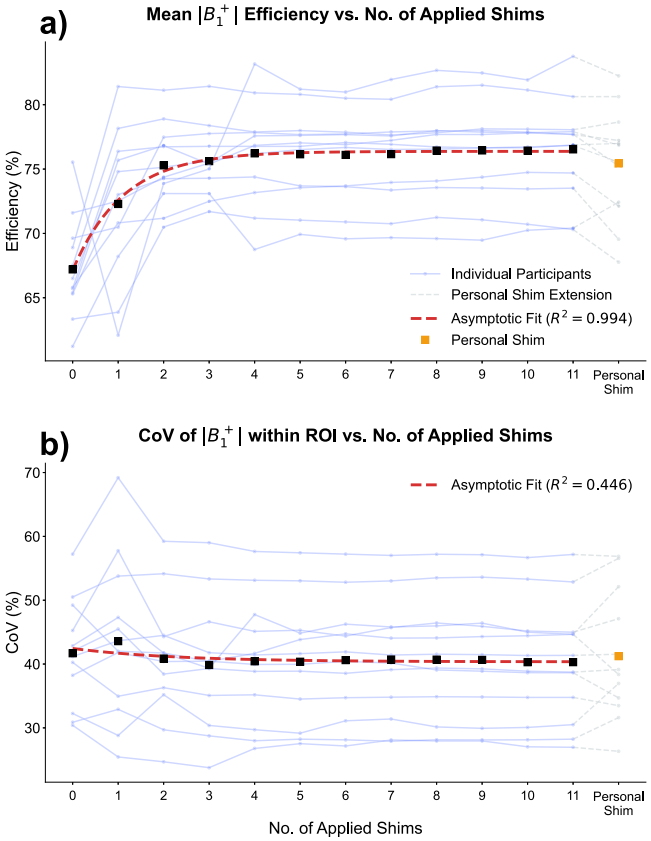



**FIGURE 2** | Gain in mean $|B_1^+|$ efficiency (%) (a) and in CoV (b) per added shim to the group optimization cohort. '0' indicates the scanner native shim setting is applied. For each individual subject, a random ordering of the 12 participants (excluding themselves) was selected. Shims were then incrementally added to the group shim from 2 to 11. Black squares indicate mean values with $x$ given shims.

normally distributed ($p > 0.05$). Analysis confirmed that both optimized shimming strategies ($\omega_p$ and $\omega_g$) outperformed the native scanner mode across all metrics except CoV, maintaining high statistical significance ($p < 0.001$ for all native comparisons). Relative to the $\omega_0$, $\omega_g$ achieved a 13.6% ± 1.1% increase in mean $|B_1^+|$ and a 3.6% ± 1.9% reduction in field CoV. Similarly, $\omega_p$ yielded improvements of 11.8% ± 1.5% in mean $|B_1^+|$ and a 1.0 ± 3.8 reduction in CoV over the native setting. Gains in transmit efficiency were also substantial, exceeding 10% for both optimized methods. Unlike in the case of the first datasets, on which the optimized shims were calculated, comparison between $\omega_g$ and $\omega_p$ on the second session data revealed almost no statistically significant differences. The personal shim showed a minor numerical decrease in Mean $|B_1^+|$ (−1.55% ± 0.71%, $p = 0.083$) and Median $|B_1^+|$ (−1.49% ± 0.86%, $p = 0.15$), though neither reached the significance threshold. The Mean transmit efficiency (−1.62% ± 0.67%, $p = 0.026$) reached the 5% significance threshold, however, the CoV (2.5% ± 2.9%, $p = 0.45$) did not. Figures S6 and S7 display swarm plots summarizing these performance results. Tables S2 and S4 display septal and voxel-ROI results from the second scan session. Figures S8 and S9 show paired subject-level low-tail, mean and median $|B_1^+|$ values for $\omega_g$, $\omega_p$, and $\omega_0$ within the whole-heart ROI for Sessions 1 and 2. To assess the generalizability of the global shim, personal shims were calculated for the six excluded participants. Figures S10 and S11 display the low-tail, mean and median $|B_1^+|$ values for the calculated shims within these six participants.

Simulations (Figure 2) show that global shimming is relatively data-efficient, with clear diminishing returns as the training-set grows. Gray traces in Figure 2 show the corresponding performance of the participant-specific personal shim. Most of the improvement in Mean $|B_1^+|$ efficiency occurred when increasing cohort size from $n = 1$ to $n = 4$, after which performance stabilized, approaching 76.4%. No clear trend in CoV was observed as additional participants were incorporated into the shim cohort. Within the whole-heart ROI, however, CoV remained relatively stable at approximately 40%, reaching 40.4% at $n = 11$, which suggests that further increases in cohort size provided little additional improvement in homogeneity. Corresponding voxel and septal results are provided in the Supplementary Material. Personal-shim performance for each participant remained close to that of global shimming, with across-participant averages of 75.4% efficiency and 41.2% CoV. Figure S12 shows the incremental performance gains within the voxel-ROI.

Direct comparison of the septum-derived and whole-heart-derived global shims showed only small differences in septal performance. The septum-derived shim provided modest additional increases in mean and median $B_1^+$ over the whole-heart shim, particularly in the second session, but did not consistently improve lower-tail $B_1^+$ or CoV. Figures S13 and S14 display these results.



15222594, 0, Downloaded from https://onlinelibrary.wiley.com/doi/10.1002/mrm.70670, Wiley Online Library on [18/11/2026]. See the Terms and Conditions (https://onlinelibrary.wiley.com/terms-and-conditions) on Wiley Online Library for rules of use; OA articles are governed by the applicable Creative Commons License

### 3.2 | In Vivo Results

Figure 3 shows representative $|B_1^+|$ maps acquired with the native mode (Figure 3a,d) and with the participant's personal (b) and global shim (e). The corresponding heat maps ((c), (f)) depict the spatial distribution of percentage change relative to the no-shim condition. The resulting global phase-only shim was $\omega_g = [-1, -8, 24, 2, 23, 52, 16, -61]^\circ$, with phases reported relative to the first transmit channel. The differences between personal shimming ($\omega_p$) and global shimming ($\omega_g$) were evaluated across 11 subjects (12 subjects included within the global test-cohort, one personalized shim scan failed). Within the septum ROI, no statistically significant advantages were observed between the two strategies for any measured metric ($p > 0.05$ for all comparisons). Specifically, Mean $|B_1^+|$ for the personal shim ($0.0514 \pm 0.0030$ Hz/V) was comparable to global shim ($0.0521 \pm 0.0026$ Hz/V, $p = 0.33$). Similarly, no significant difference was observed in $|B_1^+|$ homogeneity as measured by the CoV ($p = 0.39$). For the whole-heart ROI analysis, paired $t$-tests confirmed that $\omega_g$ remained statistically equivalent to $\omega_p$ ($p > 0.05$ for all metrics). The Median $|B_1^+|$ transmit sensitivity for $\omega_g$ was $0.0506 \pm 0.0037$ Hz/V compared to $0.0490 \pm 0.0033$ Hz/V for $\omega_p$

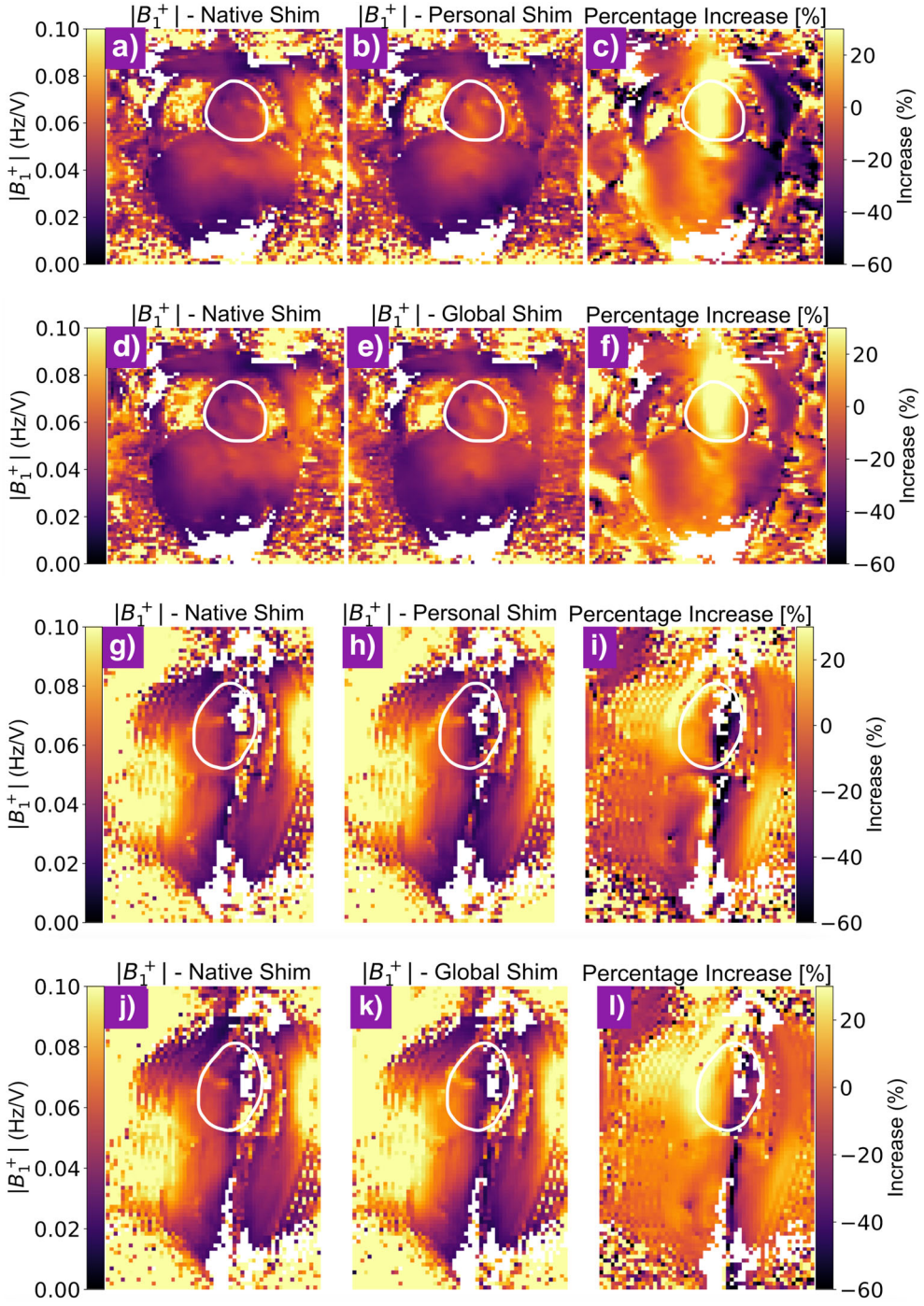



**FIGURE 3** | Representative coronal (a–f) and sagittal (g–l) $|B_1^+|$ and percentage increase maps for personal and global shimming strategies. White borders enclose the whole heart ROI.



15222594, 0, Downloaded from https://onlinelibrary.wiley.com/doi/10.1002/mrm.70670, Wiley Online Library on [18/11/2026]. See the Terms and Conditions (https://onlinelibrary.wiley.com/terms-and-conditions) on Wiley Online Library for rules of use; OA articles are governed by the applicable Creative Commons License

**TABLE 3** | Comparison of performance between $\omega_g$ and $\omega_p$ averaged across 11 volunteers.

| Improvement (%) | Global shim | Personal shim |
|---|---|---|
| Mean $\lvert B_1^+ \rvert$ (Hz/V) (whole heart) | +13.1 ± 1.0 | +11.5 ± 1.6 |
| Mean $\lvert B_1^+ \rvert$ (Hz/V) (septum) | +16.0 ± 1.9 | +14.0 ± 2.4 |
| Median $\lvert B_1^+ \rvert$ (Hz/V) (whole heart) | +17.5 ± 1.6 | +15.0 ± 2.3 |
| Median $\lvert B_1^+ \rvert$ (Hz/V) (septum) | +19.9 ± 2.5 | +17.1 ± 3.0 |
| CoV (whole heart) | −4.4 ± 1.8 | −7.0 ± 3.2 |
| CoV (septum) | −15.1 ± 3.0 | −18.8 ± 3.9 |

**TABLE 4** | Comparison of percentage improvement in performance metrics with $\omega_g$ averaged across all 18 volunteers within the whole-heart, septal, and voxel ROIs.

| ROI | Metric | % Change |
|---|---|---|
| Whole heart | $\lvert \overline{B_1^+} \rvert$ | +14.7% ± 1.2% |
| | Median $\lvert B_1^+ \rvert$ | +19.4% ± 1.4% |
| | CoV | −6.8% ± 1.9% |
| Septum | $\lvert \overline{B_1^+} \rvert$ | +17.5% ± 1.8% |
| | Median $\lvert B_1^+ \rvert$ | +22.0% ± 2.0% |
| | CoV | −15.0% ± 2.1% |
| Voxel | $\lvert \overline{B_1^+} \rvert$ | +16.2% ± 2.2% |
| | Median $\lvert B_1^+ \rvert$ | +17.4% ± 2.3% |
| | CoV | −35.0% ± 5.6% |

($p = 0.079$). Percentage improvements in transmit efficiency and homogeneity for both ROIs are summarized in Table 3.

Table 4 summarizes the changes in performance metrics within the whole heart, septal and simulated-voxel regions using the global shimming strategy in all 18 participants. While the majority of the datasets followed a normal distribution ($p > 0.05$), the $\omega_g$—$\omega_0$ difference for Mean $\lvert B_1^+ \rvert$ within the whole-heart and simulated voxel ROIs were found to be significantly non-normal (both $p = 0.035$). The Median $\lvert B_1^+ \rvert$ within the simulated voxel also followed a skewed distribution ($p = 0.049$). However, all paired-samples $t$-test and Wilcoxon signed-rank test $p$ values were found to be well below 0.001 (see Table 4). In these scanner derived $B_1^+$ maps (Figure 4), transmit optimization produced a clear and consistent shift towards higher $B_1^+$ efficiency (Hz/V) and improved homogeneity (lower CoV) across all three regions assessed. Across the cohort mean $B_1^+$ (Hz/V) increased by +14.7% ± 1.2% in the whole-heart ROI and +17.5% ± 1.8% in the intraventricular septum, with a comparable gain in the simulated voxel (+16.2% ± 2.2%). Improvements were more evident in the median $B_1^+$ (Hz/V): +19.4% ± 1.4% in the whole-heart, +22.0% ± 2.0% in the septum and +17.4% ± 2.3% in the simulated-voxel. In parallel, field inhomogeneity decreased, with CoV reduced by −6.8% ± 1.9% (whole heart), −15.0% ± 2.1% (septum), and most strongly in the simulated voxel (−35.0% ± 5.6%).

To assess the applicability of the global shimming strategy, performance metrics were assessed for a subgroup of six participants who were not included in the global shimming cohort. Using a significance threshold of $p < 0.05$, the global shim demonstrated statistically significant improvements over the native setting in all ROIs, with particularly high magnitude gains within the voxel region. In the whole heart region, improvements in Mean $\lvert B_1^+ \rvert$ efficiency (16.8% ± 3.1%, $p = 2.2 \times 10^{-3}$) and CoV (−12.2% ± 4.0%, $p = 0.019$). The septal region showed the most consistent performance, with all metrics normally distributed and $t$-test $p$ values well below 0.01. Mean $\lvert B_1^+ \rvert$ increased by 20.2% ± 4.2% ($p = 2.8 \times 10^{-3}$) and Median $\lvert B_1^+ \rvert$ increased by 26.2% ± 3.6% ($p = 4.5 \times 10^{-4}$). The 16.4% ± 3.4% reduction in CoV was also significant ($p = 0.0065$). Analysis of the voxel region revealed the greatest magnitude of change but also significant nonnormality in the distribution of performance differences. Shapiro–Wilk testing confirmed that the differences for Mean $\lvert B_1^+ \rvert$ ($p = 1.2 \times 10^{-3}$) and Median $\lvert B_1^+ \rvert$ ($p = 0.024$) were significantly skewed. However, using the nonparametric Wilcoxon-signed rank test, the $p$ value for both Mean and Median $\lvert B_1^+ \rvert$ was 0.031; within the 5% threshold. The voxel CoV demonstrated a substantial and normally distributed improvement −41.1% ± 7.5%. This met the significance threshold with a $p$ value of $8.1 \times 10^{-3}$. Table 5 summarizes these results. Figure 4 shows representative $\lvert B_1^+ \rvert$ maps for one participant acquired without shimming (a), with $\omega_g$ (b) and the corresponding heat map (c). The volunteer shown here was not included in the global shim cohort, providing an illustration of generalizability.

Figure 5 displays a representative short-axis CINE image of the heart acquired with (a) $\omega_0$ and (b) $\omega_g$. The shim provides a clear increase in image contrast, necessary for accurate voxel selection. Quantitative analysis across the full cardiac cycle (20 frames) revealed a 21% increase in mean CNR with $\omega_g$ against $\omega_0$ (10.56 vs. 8.75, respectively). Notably, the minimum CNR observed during the cycle improved by 74% (5.44 vs. 3.13), indicating that the global shim provides more robust image quality and superior myocardial border definition even during high-velocity flow phases and cardiac contraction.

Sex-specific shims produced broadly similar performance to the population-derived global shim. The male-specific shim did not provide a clear advantage, while the female-specific shim showed a modest improvement in homogeneity, most notably within the septum. Overall, the population-derived global shim performed comparably to the sex-specific alternatives. Table S5 summarizes these results.

## 4 | Discussion

In this study, we derived a global shim from the $B_1^+$ maps of 12 healthy volunteers to improve the efficiency and homogeneity of the $B_1^+$ field within the cardiac ROI. Simulations revealed that while personal shimming is theoretically superior when applied to the same session's geometry, this advantage is neutralized by within- and inter-session variability in coil-to-subject orientation. In contrast, the global shim—derived from a representative



15222594, 0, Downloaded from https://onlinelibrary.wiley.com/doi/10.1002/mrm.70670, Wiley Online Library on [18/11/2026]. See the Terms and Conditions (https://onlinelibrary.wiley.com/terms-and-conditions) on Wiley Online Library for rules of use; OA articles are governed by the applicable Creative Commons License

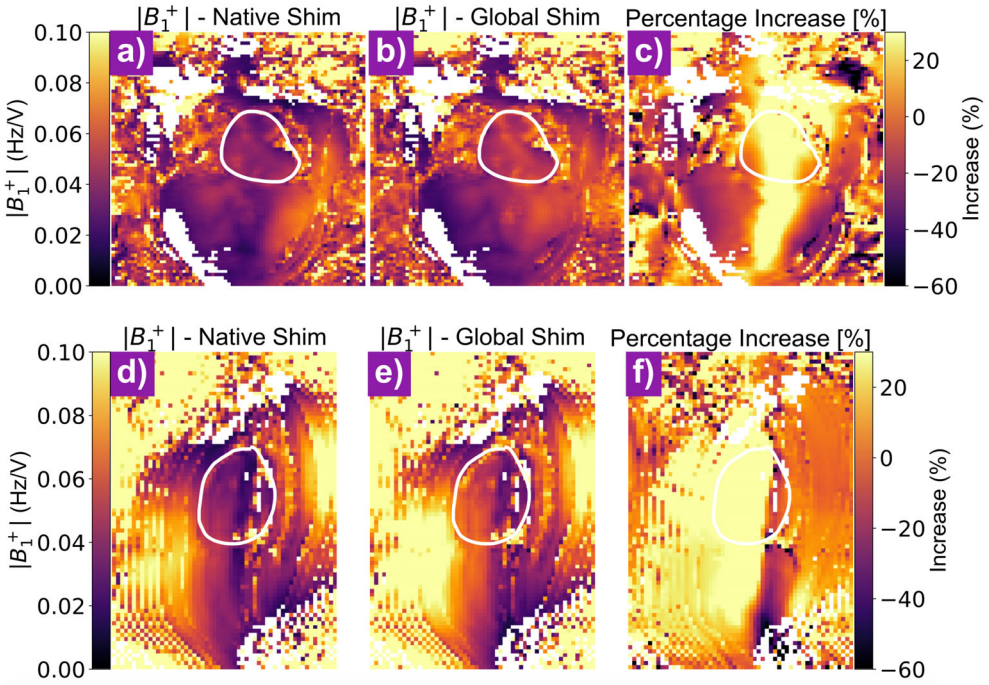



**FIGURE 4** | Representative coronal and sagittal $|B_1^+|$ maps acquired without (a), (d), and with (b), (e) "global" shim and a heat map (c), (f) shows percentage increase in $|B_1^+|$ magnitude per voxel with shim each shim. White border encloses approximate ROI of the whole heart. Participant shown not included in the optimization cohort.

**TABLE 5** | Comparison of percentage improvement in performance metrics with $\omega_g$ averaged across six volunteers not included within the optimization cohort in the whole-heart, septal, and voxel ROIs.

| ROI | Metric | % Change |
|---|---|---|
| Whole heart | $\lvert \overline{B_1^+} \rvert$ | +16.8% ± 3.1% |
| | Median $\lvert B_1^+ \rvert$ | +23.1% ± 2.4% |
| | CoV | −12.2% ± 4.0% |
| Septum | $\lvert \overline{B_1^+} \rvert$ | +20.2% ± 4.2% |
| | Median $\lvert B_1^+ \rvert$ | +26.2% ± 3.6% |
| | CoV | −16.4% ± 3.4% |
| Voxel | $\lvert \overline{B_1^+} \rvert$ | +18.3% ± 4.5% |
| | Median $\lvert B_1^+ \rvert$ | +20.0% ± 4.9% |
| | CoV | −41.1% ± 7.5% |

cohort of $N = 12$—offered a robust and significant improvement over the default mode. These findings were further corroborated by in vivo data, confirming that a fixed global strategy provides substantial gains in $B_1^+$ homogeneity and transmit efficiency without the sensitivity of a personal optimization to subject positioning and coil loading.

## 4.1 | Simulation Discussion

The comparative analysis between scan sessions highlights a critical trade-off between how well a shim fits an individual and how well it handles minor changes in positioning. In the initial simulations, the personal shim $\omega_p$ provided the theoretical ceiling for performance, as it was optimized for the exact anatomical configuration for that session. However, moving from static simulations to evaluations across sessions, the performance advantage of the personal shim was no longer evident. As expected, both optimization methods remained vastly superior to the native shim for all metrics (all $p < 0.0001$) with the exception of the CoV ($p >$ ) within the cardiac ROI (In the septal and voxel ROIs (Section S1.4), both optimized shims outperformed the native shim across all metrics, including CoV). $\omega_g$ demonstrated numerical improvements in all performance metrics over $\omega_p$, though only the mean transmit efficiency proved statistically significant ($p = 0.026$). This suggests that the advantage of a personalized shim may be highly sensitive to changes in anatomy-to-coil orientation; once the participant moves or is removed and replaced in the bore, the slight shifts in anatomy-to-coil orientation negate the fine-tuned benefits of the personal optimization. So while a personalized shim provides the best performance for the specific anatomy and position for which it was optimized, a global shim may sacrifice some personal optimality in favor of greater robustness to positional and anatomical variation. The observation that the global shim performed at least as well as the personalized shim across sessions may therefore reflect its reduced sensitivity to changes in anatomy-to-coil orientation. By optimizing for a cohort of 12 subjects, the global shim effectively "averages" anatomical variations, making it more resilient to the geometric sensitivity of high-field MRI. In the whole-heart ROI, the corresponding reduction in CoV was small compared with the substantial improvement in $B_1^+$ efficiency. These results suggest that, under the present phase-only optimization framework and coil configuration, the achievable reduction in spatial variation was limited, whereas efficiency could be improved more consistently (see Section S1.2).



15222594, 0, Downloaded from https://onlinelibrary.wiley.com/doi/10.1002/mrm.70670, Wiley Online Library on [18/11/2026]. See the Terms and Conditions (https://onlinelibrary.wiley.com/terms-and-conditions) on Wiley Online Library for rules of use; OA articles are governed by the applicable Creative Commons License

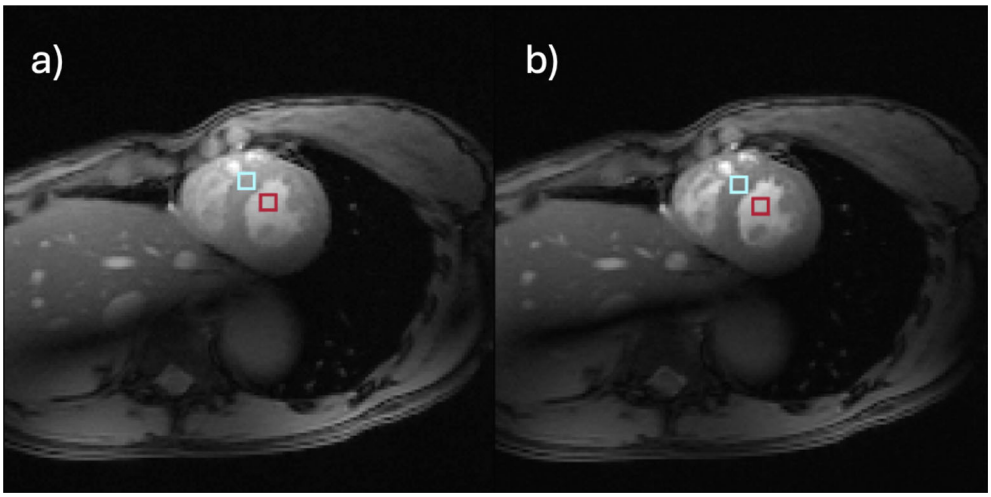



**FIGURE 5** | Representative CINE images with the (a) native shim and with the (b) global shim. The red and blue squares indicate the blood-pool and septum regions used to calculate the CNR respectively.

### 4.2 | In Vivo Discussion

The evolution of shimming performance as subjects were incrementally added to the global shimming group ($N = 1 – N = 11$) demonstrates that both $|\overline{B_1^+}|$ efficiency and the CoV exhibited clear diminishing returns as the cohort expanded. The most substantial improvements in transmit efficiency were realized within the first four subjects. Beyond this threshold, the performance metrics reached a stable plateau, with negligible gains observed as the cohort reached a size of $N = 11$. This asymptotic behavior suggests that the primary spatial variations of the $B_1^+$ field—dictated by the shared characteristics of human body anatomy—are effectively encapsulated by a relatively small representative group. Additionally, the personal shim underperformed relative to the established global plateau seen in Figure 2 when applied to the second scan session, as expected from the simulations. Specifically, the mean efficiency of the personal shim dropped below the asymptotic level achieved by the $N = 11$ cohort, while its CoV rose above the global homogeneity plateau. This suggests that $\omega_p$ is so "overfit" to the specific geometry of the first scan that it lacks the spatial bandwidth to accommodate the minor anatomical shifts inherent to re-scanning. It would be impractical to perform the optimization whilst the participant was still in the scanner, adding $\geq 20$ min to the scan time. Even so, a new personal shim would only significantly outperform $\omega_g$ if the participant remained stationary for the full 45-min scan. In contrast, optimization over a heterogeneous cohort ($N = 11$) including both sexes and a broad range of BMI produces a global shim that is less sensitive to inter-subject differences in geometry and loading, and therefore remains effective across a wider range of anatomies. This may also make it more robust to small intra-scan movements, as well as inter-session repositioning. This "performance crossover"—where the generalized $\omega_g$ outperforms the specialized $\omega_p$—reinforces the practical utility of the diminishing returns analysis. The argument for $\omega_g$ is further strengthened given that with a skewed distribution of efficiencies ($p = 0.040$), it remained significantly more effective and stable than the scanner's native settings ($p < 0.001$).

A cohort of 12 subjects was sufficient to provide a "statistically saturated" global shim which generalizes well to unseen participants without requiring further anatomical data (Table 5). This is revealed by the significant performance gains observed across the six subjects not included in the global cohort. When evaluated against a stringent 1% significance threshold, the global shim demonstrated its most reliable impact in the septal region, where all metrics reached significance ($p \leq 6.5 \times 10^{-3}$). While the voxel-wise analysis yielded the highest magnitude of change—specifically a $41.1\% \pm 7.5\%$ reduction in CoV ($p = 8.1 \times 10^{-3}$)—it also exhibited the most significant skewness in $|B_1^+|$ magnitude differences. The nonnormality observed in voxel Mean $|B_1^+|$ ($p = 0.012$) and Median $|B_1^+|$ likely reflects the high sensitivity of localized regions to individual anatomical variations. In contrast, the whole-heart ROI integrates values over a larger volume, resulting in more Gaussian-distributed improvements ($p > 0.05$, Shapiro–Wilk), though the overall efficiency gain (16.8%) was lower than that of the septum. The fact that a generalized shim solution—calculated entirely from a separate cohort—could produce a significant 20% boost in septal $B_1^+$ and a 41% improvement in voxel homogeneity in new participants is a powerful argument for a "global" shim. Despite the minor skewness in localized metrics, the consistent performance across anatomical regions validates the global shim as a robust strategy which effectively captures the dominant $B_1^+$ patterns of the human torso at 7 T.

Our results hence suggest that the global shim represents a more efficient and robust strategy for cardiac $B_1^+$ shimming at 7 T compared to personal shimming. While statistical analysis confirmed that $\omega_g$ is comparable to $\omega_p$ (all $p > 0.05$), $\omega_g$ consistently demonstrated a numerical lead in transmit efficiency across both regions of interest. Notably, $\omega_g$ achieved a $+17.5\% \pm 1.6\%$ increase in whole-heart ROI median $|B_1^+|$, out-performing the $+15.0\% \pm 2.3\%$ improvement observed with $\omega_p$. This trend was maintained in the septum (+19.9% vs. +17.1%), suggesting that the global solution is less sensitive to ROI selection, and provides superior consistency in transmit efficiency across different anatomical cardiac regions. Although $\omega_p$ showed a



15222594, 0, Downloaded from https://onlinelibrary.wiley.com/doi/10.1002/mrm.70670, Wiley Online Library on [18/11/2026]. See the Terms and Conditions (https://onlinelibrary.wiley.com/terms-and-conditions) on Wiley Online Library for rules of use; OA articles are governed by the applicable Creative Commons License

marginal numerical advantage in CoV reduction (e.g., −18.8% vs. −15.1% in the septum), this result was not statistically significant. These slight gains in uniformity likely represent a point of diminishing returns; they require additional, time-consuming steps for subject-dependent mapping and optimization without yielding a measurable performance benefit over the global shim. The additional analyses suggest that the population-derived whole-heart shim is relatively insensitive to subdivision of the optimization cohort or restriction of the optimization ROI. Septum-specific optimization produced only a small additional gain, while sex-specific shims offered little consistent advantage over the global solution. The statistical equivalence between the two solutions indicates that the significant time and computational work required for personal shimming is not justified for routine use. Consequently, $\omega_g$ offers a robust alternative that simplifies workflow without sacrificing $B_1^+$ performance. Previous work by Egger et al. [6] demonstrated the feasibility of universal cardiac RF shimming at 7 T. The present study extends this by evaluating robustness across repeated acquisitions and an independent validation cohort, assessing performance within spectroscopy-relevant ROIs, comparing a global shim with personalized shims derived from a separate scan session, and providing proof-of-concept in vivo cardiac $^1$H MRI.

The benefits of a global shim are not confined to anatomical CINE imaging (Figure 5) but are also applicable to more demanding applications, such as cardiac proton spectroscopy. Cardiac MRS voxels often encompass a mixture of the intraventricular septum and the adjacent blood pool to maximize signal and account for cardiac motion. In this context, achieving uniform excitation across the entire voxel volume is critical for reliable metabolite quantification. Furthermore, the 74% improvement in minimum CNR ensures that the myocardial-blood interface remains well-defined throughout the cycle. This enhanced visibility is essential for precise voxel positioning and for accurately characterizing the tissue proportions within the localized volume, thereby reducing variability in the resulting metabolic profiles.

Ultimately, an improvement in SNR and $B_1^+$ homogeneity may aid quantification of cardiac metabolites such as Cho and Cr, carnosine and acetyl-carnitine, which are relevant markers of cardiac metabolism and health [14]. At 7 T, cardiac MRS is especially sensitive to $B_1^+$ homogeneity, which can lead to significant errors in metabolite quantification. In the simulated myocardial MRS voxel, $\omega_g$ significantly outperformed $\omega_0$, increasing Mean and Median $B_1^+$ by 16.2% and 17.4%, respectively, while reducing CoV by 35.0%. This reduction in spatial variation is particularly critical for spectroscopy, where nonuniform excitation can introduce metabolite quantification errors. While the $B_1^+$ magnitude improvements in this localized region showed some skewness ($p = 0.049$ for Mean $|B_1^+|$), the performance remained significantly superior to the default system shim ($p = 7.63 \times 10^{-6}$, Wilcoxon). These improvements are especially relevant for STEAM, which requires three accurate 90° RF pulses and is therefore sensitive to both insufficient transmit efficiency and spatial $B_1^+$ variation. The increased Median $|B_1^+|$ facilitates the required flip angles without exceeding power limits, whilst the reduced CoV helps maintain uniform excitation across the localized volume.

## 5 | Conclusions

Although personal RF-shimming defines the optimal case for the specific anatomy-to-coil configuration used for optimization, its advantage is sensitive to scan-rescan positioning differences. Building on previous demonstrations of universal cardiac phase shimming at 7 T, this study provides further prospective evidence for the robustness and practical utility of a population-derived global shim across independent participants and repeated scan sessions. In simulation, the population-derived "global" shim achieved transmit sensitivity and homogeneity within 3% of the personal shim. Asymptotic analysis further suggested that the global shim performance stabilized after the inclusion of only a small number of training subjects. By compensating for these recurring phase cancelations, the global shim retained much of the performance gain without requiring per-subject calibration. Theoretical improvements were also observed within spectroscopy-relevant septal and voxel ROIs, supporting the potential use of a fixed global shim for cardiac MRI and MRS applications at 7 T. These findings have a dual impact on ultra-high field infrastructure. For active parallel-transmit (pTx) systems, the global shim reduces reliance on online optimization. At the same time, for multi-nuclear applications which are restricted to sTx hardware, it offers a practical route to improving baseline coil performance through fixed combined transmit mode. In practice, the phase relationships defined by the global shim could be implemented using fixed cable-length offsets, providing a predetermined $^1$H transmit mode that could be used alongside a $^3$1P spectroscopy coil without requiring subject-specific pTx optimization. Overall, these results support the use of a population-derived global shim as a reproducible and operationally simple strategy for cardiac metabolic research at 7 T.

### 5.1 | Limitations

The study cohort was relatively small ($N = 12$ in simulations, $N = 6$ for validation) and consisted of healthy volunteers. However, the "saturation" analysis (Figure 2) demonstrated that the global shim weights stabilized by subject ∼4, suggesting that a larger healthy cohort would yield diminishing returns. The optimization maximized the transmit sensitivity (Hz/V), transmit efficiency (%), and homogeneity (CoV, %), but did not include full electromagnetic simulations for local Specific Absorption Rate supervision. The scanner-reported SAR estimates do not correspond to subject-specific peak local 10 g-averaged SAR. Subject-specific electromagnetic simulations, Q-matrices, or VOPs were not available; therefore, local SAR regularization was not included in the optimization and peak local SAR could not be estimated retrospectively. Instead, the coil was operated under the scanner's conservative worst-case per-channel power limits, which were independent of the applied phase vector. Improvements in Transmit Sensitivity reduce the input power required to achieve a given flip angle and would therefore be expected to reduce the global SAR burden, although this was not directly quantified here. For the cohort-size analysis, a single random ordering of the available training subjects was used for each held-out participant. As a result, the analysis provides an estimate of the effect of increasing cohort size using representative random



15222594, 0, Downloaded from https://onlinelibrary.wiley.com/doi/10.1002/mrm.70670, Wiley Online Library on [18/11/2026]. See the Terms and Conditions (https://onlinelibrary.wiley.com/terms-and-conditions) on Wiley Online Library for rules of use; OA articles are governed by the applicable Creative Commons License

training cohorts, but does not fully quantify the sensitivity of the results to different possible subject orderings.


## Funding

This work was supported by the Sir Henry Dale Fellowship of the Wellcome Trust and the Royal Society (221805/Z/20/Z), British Heart Foundation (FS/19/18/34252), and by the Slovak Grant Agencies VEGA (2/0084/26) and APVV (21-0299). This research was supported by the NIHR Oxford Health Biomedical Research Centre (NIHR203316). The Centre for Integrative Neuroimaging was supported by core funding from the Wellcome Trust (203139/Z/16/Z and 203139/A/16/Z). We also thank the UK BBSRC (grant number BB/W019582/1) for support. The views expressed are those of the author(s) and not necessarily those of the NIHR or the Department of Health and Social Care.


## Conflicts of Interest

The authors declare no conflicts of interest.

## Data Availability Statement

The data and optimization code that support the findings of this study are available here https://doi.org/10.5281/zenodo.22130485.

## References


1. C. J. Snyder, L. DelaBarre, G. J. Metzger, et al., "Initial Results of Cardiac Imaging at 7 Tesla," *Magnetic Resonance in Medicine* 61, no. 3 (2009): 517–524, https://onlinelibrary.wiley.com/doi/pdf/10.1002/mrm.21895.

2. S. Herz, M. R. Stefanescu, D. Lohr, et al., "Effects of Image Homogeneity on Stenosis Visualization at 7 T in a Coronary Artery Phantom Study: With and Without B1-Shimming and Parallel Transmission," *PLoS One* 17, no. 6 (2022): e0270689, https://doi.org/10.1371/journal.pone.0270689.

3. J. L. Kent, I. Dragonu, L. Valkovič, and A. T. Hess, "Rapid 3D Absolute B1+ Mapping Using a Sandwiched Train Presaturated TurboFLASH Sequence at 7 T for the Brain and Heart," *Magnetic Resonance in Medicine* 89, no. 3 (2023): 964–976, https://onlinelibrary.wiley.com/doi/pdf/10.1002/mrm.29497.

4. M. Terekhov, I. A. Elabyad, and L. M. Schreiber, "Global Optimization of Default Phases for Parallel Transmit Coils for Ultra-High-Field Cardiac MRI," *PLoS One* 16, no. 8 (2021): e0255341, https://doi.org/10.1371/journal.pone.0255341.

5. C. S. Aigner, S. Dietrich, T. Schaeffter, and S. Schmitter, "Calibration-Free pTx of the Human Heart at 7T via 3D Universal Pulses," *Magnetic Resonance in Medicine* 87, no. 1 (2022): 70–84, https://doi.org/10.1002/mrm.28952.

6. E. Nico, N. Sophia, W. Saskia, et al., "Accelerated B 1 + $B_1^+$ Mapping and Robust Parallel Transmit Pulse Design for Heart and Prostate Imaging at 7T," *Magnetic Resonance in Medicine* 92, no. 5 (2024): 1933–1951.

7. C. S. Aigner, F. Sánchez Alarcon Manuel, D'A. Alexandre, A.-O. Eva, C.-A. Julien, and S. Sebastian, "Calibration-Free Parallel Transmission of the Cervical, Thoracic, and Lumbar Spinal Cord at 7T," *Magnetic Resonance in Medicine* 92, no. 4 (2024): 1496–1510, https://onlinelibrary.wiley.com/doi/pdf/10.1002/mrm.30137.

8. B. Adam, P. Michal, M. Christopher, et al., "Calibration-Free Regional RF Shims for MRS," *Magnetic Resonance in Medicine* 86, no. 2 (2021): 611–624, https://doi.org/10.1002/mrm.28749.

9. M. M. Garcia, K. T. Chaim, M. C. Otaduy, et al., "Investigating the Influence of Dielectric Pads in 7T Magnetic Resonance Imaging–Simulated and Experimental Assessment," *Current Directions in Biomedical Engineering* 6, no. 3 (2020): 24–27, https://doi.org/10.1515/cdbme-2020-3007.

10. E. Gabriele and G. Matthias, "Local Specific Absorption Rate Control for Parallel Transmission by Virtual Observation Points," *Magnetic Resonance in Medicine* 66, no. 5 (2011): 1468–1476, https://doi.org/10.1002/mrm.22927.

11. A. A. Hurshkainen, S. Bart, S. B. Glybovski, et al., "A Parametric Study of Radiative Dipole Body Array Coil for 7 Tesla MRI," *Photonics and Nanostructures—Fundamentals and Applications* 39 (2020): 100764, https://doi.org/10.1016/j.photonics.2019.100764.

12. F. Tobias, H. Fabian, R. Wolfgang, et al., "Acoustic Cardiac Triggering: A Practical Solution for Synchronization and Gating of Cardiovascular Magnetic Resonance at 7 Tesla," *Journal of Cardiovascular Magnetic Resonance: Official Journal of the Society for Cardiovascular Magnetic Resonance* 12, no. 1 (2010): 67, https://doi.org/10.1186/1532-429X-12-67.

13. J. Mark, C. F. Beckmann, T. E. J. Behrens, W. Woolrich Mark, and M. Smith Stephen, "FSL," *NeuroImage* 62, no. 2 (2012): 782–790, https://doi.org/10.1016/j.neuroimage.2011.09.015.

14. I. M. Zubair, B. Dennis, S. Andrea, et al., "Association of Gut-Related Metabolites With Outcome in Acute Heart Failure," *American Heart Journal* 234 (2021): 71–80, https://doi.org/10.1016/j.ahj.2021.01.006.


## Supporting Information

Additional supporting information can be found online in the Supporting Information section. **Figure S1:** Whole-heart ROI performance for increasing homogeneity weighting, from $\lambda_{cov} = 0$ (no homogeneity optimisation) to $\lambda_{cov} = 100$ (strongest homogeneity weighting) using $\lambda_{cov}$ from Equation (2). Personal shim uses $\lambda_{cov} = 0.5$. **Figure S2:** Absolute circular phase differences between each personalised shim ωp,i, where i denotes the subject in the optimisation cohort, and the global shim ωg across the eight transmit channels. Shims are ranked from closest to furthest from the global shim according to their mean absolute circular phase difference. **Figure S3:** Absolute circular phase difference between each personal shim ωp,i and the global shim ωg for each of the eight transmit channels. Each line represents one personal shim, allowing direct visual comparison of how the phase-vector differences vary across channels. Shims closer to zero across all channels are more similar to the global shim, while larger deviations indicate greater divergence from the global phase solution. **Figure S4:** Phase differences between each personal shim ωp,i, where i denotes the subject in the optimisation cohort, and the global shim ωg across the eight transmit channels. Shims are ranked from closest to furthest from the global shim according to their mean absolute circular phase difference. **Figure S5:** Phase differences between each personal shim ωp,i, where i denotes the subject in the optimisation cohort, and the global shim ωg across the eight transmit channels. **Figure S6:** Comparison of B1+ performance across voxel, septal and whole-heart regions of interest in the first scan session. Swarm plots show subject-level mean B1+, median B1+, mean B1+ efficiency, and coefficient of variation of B1+ for the native, personal and global shim conditions. Rows correspond to the voxel, septal and whole-heart regions of interest. **Figure S7:** Comparison of B1+ performance across voxel, septal and whole-heart regions of interest in the second scan session. Swarm plots show subject-level mean B1+, median B1+, mean B1+ efficiency, and coefficient of variation of B1+ for the native, personal and global shim conditions. Rows correspond to the voxel, septal and whole-heart regions of interest. **Table S1:** Performance metrics from simulations from the first scan session. Changes with 'personal' (P) and 'global' (G) shims relative to the scanner native (nat) system shim within the septal ROI are shown. Absolute changes are reported alongside relative percentage changes. Values represent averages across the 12 participants included in




15222594, 0, Downloaded from https://onlinelibrary.wiley.com/doi/10.1002/mrm.70670, Wiley Online Library on [18/11/2026]. See the Terms and Conditions (https://onlinelibrary.wiley.com/terms-and-conditions) on Wiley Online Library for rules of use; OA articles are governed by the applicable Creative Commons License

the optimisation cohort. **Table S2:** Performance metrics from simulations from the second scan session. Changes with 'personal' (P) and 'global' (G) shims relative to the system native (nat) shim mode within the septal ROI are shown. Absolute changes are reported alongside relative percentage changes. Values represent averages across the 12 participants included in the optimisation cohort. **Table S3:** Performance metrics from simulations from the first scan session. Changes with 'personal' (P) and 'global' (G) shims relative to the scanner native (nat) system shim within the voxel ROI are shown. Percentage changes are reported. Values represent averages across the 12 participants included in the optimisation cohort. **Table S4:** Performance metrics from simulations from the second scan session. Changes with 'personal' (P) and 'global' (G) shims relative to the scanner native (nat) system shim within the voxel ROI are shown. Absolute changes are reported alongside relative percentage changes. Values represent averages across the 12 participants included in the optimisation cohort. **Figure S8:** Paired subject-level P5 and P10 |B1+| values for the native, global and personal shim conditions in the 12 participants within the whole-heart ROI for both sessions 1 and 2. Lines connect measurements from the same participant. Black points indicate the group mean and error bars show mean ± SEM. **Figure S9:** Paired subject-level mean and median |B1+| values for the native, global and personal shim conditions in the 12 participants within the whole-heart ROI. Lines connect measurements from the same participant. Black points indicate the group mean and error bars show mean ± SEM. **Figure S10:** Paired subject-level P5 and P10 |B1+| values for the native, global and personal shim conditions in the 6 excluded validation participants within the whole-heart ROI. Lines connect measurements from the same participant. Black points indicate the group mean and error bars show mean ± SEM. **Figure S11:** Paired subject-level mean and median |B1+| values for the native, global and personal shim conditions in the 6 excluded validation participants within the whole-heart ROI. Lines connect measurements from the same participant. Black points indicate the group mean and error bars show mean ± SEM. **Figure S12:** Mean |B1+| efficiency and (b) CoV of |B1+| are plotted against the number of shim vectors included in the incremental global shim calculation within the voxel ROI. Light-blue lines show individual participants ($n = 12$), while black squares show the cohort mean. Red dashed curves represent asymptotic fits to the cohort means, with R2 values reported in the legends. Gray dashed lines connect the final incremental result to each participant's independently optimised personal shim at position 12, and the orange square represents the cohort-mean personal-shim performance. Diamonds indicate additional shim optimisations obtained using CoV weighting parameters of 0, 10, and 100. **Figure S13:** Comparison of whole-heart and septum-derived global shims within the septal ROI. Percentage improvement in mean and median |B1+| relative to the native shim is shown for the whole-heart-derived and septum-derived global shims during Session 1 (a,b) and Session 2 (c,d). Colored lines connect paired measurements from the same participant. Black points indicate the group mean and error bars show mean ± SEM. **Figure S14:** Lower-tail |B1+| performance of whole-heart- and septum-derived global shims within the septal ROI. Fifth-percentile (P5) and tenth-percentile (P10) |B1+| values are shown for the native, whole-heart-derived global and septum-derived global shim configurations during Session 1 (a,b) and Session 2 (c,d). Colored lines connect measurements from the same participant. Black points indicate the group mean and error bars show mean ± SEM. **Table S5:** Comparison of global and personal group shim performance within the whole-heart (W), septal (S), and spectroscopy-voxel (V) ROIs from scanner-derived B1+ maps. Values are reported as mean percentage change ± SEM from ωg to ωp. Positive changes in mean and median B1+ indicate higher B1+ with the personal shim, whereas negative changes in CoV indicate improved homogeneity. Star denotes significant result.



15222594, 0, Downloaded from https://onlinelibrary.wiley.com/doi/10.1002/mrm.70670, Wiley Online Library on [18/11/2026]. See the Terms and Conditions (https://onlinelibrary.wiley.com/terms-and-conditions) on Wiley Online Library for rules of use; OA articles are governed by the applicable Creative Commons License